The Astrophysical Journal Letters, 898:L30 (11pp), 2020 August 1 https://doi.org/10.3847/2041-8213/aba199

Hidden AGNs in Dwarf Galaxies Revealed by MaNGA: Light Echoes, Off-nuclear Wanderers, and a New Broad-line AGN

Mar Mezcua[1,2] and Helena Domínguez Sánchez[1]
[1] Institute of Space Sciences (ICE, CSIC), Campus UAB, Carrer de Magrans, E-08193 Barcelona, Spain; marmezcua.astro@gmail.com
[2] Institut d'Estudis Espacials de Catalunya (IEEC), Carrer Gran Capità, E-08034 Barcelona, Spain
Received 2020 April 24; revised 2020 June 28; accepted 2020 June 30; published 2020 July 28

Abstract

Active galactic nuclei (AGNs) in dwarf galaxies could host the relics of those early universe seed black holes that did not grow into supermassive black holes. Using MaNGA integral field unit (IFU) spectroscopy we have found a sample of 37 dwarf galaxies that show AGN ionization signatures in spatially resolved emission line diagnostic diagrams. The AGN signatures are largely missed by integrated emission line diagnostics for 23 of them. The bolometric luminosity of these 23 new AGN candidates is $\lesssim 10^{40}$ erg s^{-1}, fainter than that of single-fiber SDSS AGNs, X-ray AGNs, and radio AGNs in dwarf galaxies, which supports IFU spectroscopy as a powerful tool for identifying hidden and faint AGNs in dwarf galaxies. The AGN emission is in most cases offset from the optical center of the dwarf galaxy and shows a symmetric morphology, which indicates that either the AGNs are off-nuclear, that the central emission of the galaxy is dominated by star formation, or that the AGNs are turned off and we are observing a past ionization burst. One of the new AGNs shows a broad Hα emission line component, from which we derive a black hole mass in the realm of intermediate-mass black holes. This constitutes the first hidden type 1 AGN discovered in a dwarf galaxy based on IFU spectroscopy. The finding of this sample of hidden and faint AGNs has important implications for population studies of AGNs in dwarf galaxies and for seed black hole formation models.

Unified Astronomy Thesaurus concepts: Active galactic nuclei (16); Dwarf galaxies (416)

Supporting material: figure set

1. Introduction

The finding of hundreds of active galactic nuclei (AGNs) in low-mass dwarf galaxies (stellar mass $M_* \leqslant 3 \times 10^9\ M_\odot$) has revolutionized black hole and galaxy formation models. These AGNs are often found to be powered by low-mass or intermediate-mass black holes (IMBHs; $100 < M_{\rm BH} \lesssim 10^6\ M_\odot$), which could be the relics of the early universe seed black holes from which supermassive black holes ($M_{\rm BH} > 10^6\ M_\odot$) grow (see Mezcua 2017; Greene et al. 2019 for recent reviews). If these seeds have not significantly grown by mergers or AGN feedback through cosmic time (Mezcua 2019, 2020), characterizing the local population of IMBHs in dwarf galaxies, in particular the black hole occupation fraction and the low-mass end of the scaling relations, can tell us how seed black holes predominantly formed at $z > 10$ (e.g., van Wassenhove et al. 2010; Ricarte & Natarajan 2018).

Myriad studies have hence focused on identifying AGNs in dwarf galaxies. The first searches were based on optical spectroscopic surveys such as the Sloan Digital Sky Survey (SDSS[3]) and the use of narrow emission line diagnostic diagrams (BPT diagrams; Baldwin et al. 1981; Kewley et al. 2001, 2006; Kauffmann et al. 2003) to distinguish between gas ionization by AGNs or by stars, accompanied by the detection of broad Balmer emission lines from which a black hole mass measurement could be obtained (e.g., Reines et al. 2013; Moran et al. 2014). Such optical studies are, however, biased toward central luminous type 1 AGNs with high accretion rates and at low redshifts ($z < 0.3$). This can be circumvented by X-ray and radio searches, which are not only able to detect AGNs in dwarf galaxies at the pinnacle of cosmic star formation history (Mezcua et al. 2016, 2018a, 2019), but offer the most reliable measurements of the AGN fraction in dwarf galaxies (e.g., Mezcua et al. 2018a; Birchall et al. 2020).

In addition to the biases of optical searches, single-fiber BPT diagnostics can fail at identifying AGNs in dwarf galaxies with active star formation (e.g., Cann et al. 2019; Birchall et al. 2020) or with a strong host galaxy light that dilutes the AGN signatures (e.g., Moran et al. 2002). This can be circumvented by high-resolution optical spectroscopy (e.g., Dickey et al. 2019) or optical variability studies (e.g., Baldassare et al. 2018, 2020), which are able to reveal AGN signatures even in quiescent and star formation-dominated dwarf galaxies.

The advent of integral-field unit (IFU) spectroscopic surveys such as SDSS/MaNGA (Mapping Nearby Galaxies at APO; Bundy et al. 2015) has opened a new window in the identification of "hidden" AGNs (e.g., Wylezalek et al. 2018). Such sources are missed by single-fiber BPT diagnostics if other mechanisms rather than the AGN dominate the ionization at the galaxy center, if the AGN is displaced from the central region due to a galaxy merger (e.g., Comerford & Greene 2014; Barrows et al. 2018), or if the AGN has recently switched off and its ionization signatures are only observable as light echoes at large distances from the optical center (e.g., Keel et al. 2015). Yet, most AGN searches using IFU data are biased toward central AGNs or do not focus on dwarf galaxies (Rembold et al. 2017; Sánchez et al. 2018; Wylezalek et al. 2018). Penny et al. (2018) used the MaNGA survey to investigate AGNs in dwarf galaxies, but their sample included only 69 quenched systems. Hence, no systematic studies of AGNs in dwarf galaxies has been performed so far using IFU data.

[3] https://www.sdss.org

In this Letter we present the largest dedicated study of AGNs in dwarf galaxies using MaNGA data of 4718 sources. This allows us to identify AGN candidates in 37 dwarf galaxies, in 23 of which no clear AGN signatures are revealed in the single-spectrum BPT, and includes the discovery of a new broad-line low-mass AGN. The sample and analysis are presented in Section 2, while the results obtained are discussed in Section 3. Conclusions are provided in Section 4.

2. Sample and Analysis

The sample of dwarf galaxies studied in this paper is drawn from the SDSS/MaNGA survey Data Release[4] 15, which includes 4718 galaxies. The MaNGA IFU is centered on the optical center of the galaxy and has a size that typically matches the angular size of the galaxy, so that most targets are covered spectroscopically to at least 1.5 effective radii ($R_{\rm eff}$). The final data cubes provided by the MaNGA data-analysis pipeline[5] have square spaxels $0\farcs5$ in size, and the median spatial resolution is of $2\farcs5$ full width at half maximum (FWHM). We use the emission line measurements (performed after subtraction of the stellar continuum and corrected for absorption) of the HYB10-GAU-MILESHC maps, in which the spaxels are binned to a signal-to-noise ratio (S/N) $\sim$ 10 but the kinematic properties are extracted from the individual spaxels.

We also take from the MaNGA data-analysis pipeline the star formation rate (SFR) within the IFU field of view based on the Hα flux and the flux-weighted mean stellar velocity dispersion (σ) of all spaxels within 1 $R_{\rm eff}$.

$R_{\rm eff}$, redshift (z), and M_* are taken from the NASA–Sloan Atlas (NSA catalog) version v1_0_1, as used by MaNGA for its targeting,[6] which incorporates an expanded redshift range and an improved elliptical Petrosian aperture photometry compared to the previous NSA catalog v0_1_2. The SFR and M_* are provided in units of $h^{-2}\ M_\odot\ {\rm yr}^{-1}$ and $h^{-2}\ M_\odot$, respectively, and we assume $h = 0.73$.

To draw our sample we first select those sources for which the Petrosian and Sérsic NSA stellar masses are consistent within 0.5 dex (e.g., Secrest & Satyapal 2020). The target dwarf galaxies are then selected as having $M_* < 3 \times 10^9\ M_\odot$, as commonly done in AGN studies of dwarf galaxies (e.g., Reines et al. 2013, 2020; Mezcua et al. 2018a, 2019). No magnitude cut is applied to avoid any biases toward galaxy type. This yields an initial sample of 1609 dwarf galaxies.

To identify the source of ionization of each spaxel we use the lines of Kewley et al. (2001, 2006) and Kauffmann et al. (2003) to distinguish between AGNs, star formation, or composite (combination of AGN and star formation ionization) in the [O III]/H$_\beta$ versus [N II]/H$_\alpha$ ([N II]-BPT) and [O III]/H$_\beta$ versus [S II]/H$_\alpha$ ([S II]-BPT) emission line diagnostics. We also use the line from Schawinski et al. (2007) for a LINER[7] division in the [N II]-BPT. We only consider those dwarf galaxies for which the S/N of the lines used in the [N II]-BPT and [S II]-BPT diagrams (H$_\alpha$, H$_\beta$, [N II]λ6583, [S II]λ6718, [O III]λ5007) is $\geqslant$3. For these we first plot the [N II]-BPT and [S II]-BPT and select those galaxies for which at least 5 spaxels are located in the AGN/LINER photoionization region of both these diagram (see Figure 1, top left panel). Then, for each galaxy, the individual spectra of all the spaxels identified as AGNs or LINERs according to the above criteria are stacked together in order to increase the signal. The stacking procedure is explained in detail in Appendix A. Those sources whose stacked spectrum is very noisy and/or for which the emission lines of interest are hardly identifiable or have inconsistent measurements are removed from the sample. We also exclude those galaxies for which the spaxels classified as AGN/LINER are spread at the edges of the S/N $>$ 1 continuum map (gray area in Figure 1, top middle panel). This yields a sample of 102 AGN dwarf galaxy candidates.

We derive a median BPT location of the 102 AGN candidates by taking the median of the [N II]-BPT line fluxes of the same AGN/LINER spaxels used to obtain the stacked spectrum (black square in Figure 1, top left panel). Based on this median BPT location, 47 of the AGN candidates are classified as LINERs. The LINER emission can not only originate from AGNs but also be produced on galactic scales by hot old stars, which are expected to have an Hα equivalent width (EW) typically below 3 Å. A distinction between the two processes can be made using the WHAN diagram (Cid Fernandes et al. 2010), which suggests that sources with EW(Hα) $>$ 3 Å and flux ratio log [N II]/Hα $>$ -0.4 can be classified as true AGNs. A further sub-classification can be performed among strong AGNs (EW(Hα) $>$ 6 Å) and weak AGNs (3 Å $<$ EW(Hα) $<$ 6 Å; see Figure 2). Based on the WHAN diagram of the median value of the AGN/LINER spaxels and relaxing the EW(Hα) cut to $>$2.8 Å in order not to exclude bona fide AGNs (see Section 3), we find that the AGN/LINER spaxels of 37 out of the 102 AGN candidates are consistent with being dominated by AGN ionization. These 37 sources constitute our final sample of AGN dwarf galaxy candidates.

3. Results and Discussion

Of the 37 AGN candidates identified above using MaNGA data, 36 have also single-fiber (3″ aperture) SDSS spectra available. For one of the sources (9881-1901) the Hα region is missing, so we consider only 35 SDSS spectra. Two of them (8446-1901 and 9000-1901) are known broad-line AGNs (e.g., Reines & Volonteri 2015, from which we take the narrow emission line fluxes to obtain the SDSS BPT classification), while for the remaining 33 sources we obtain an SDSS BPT classification based on the emission line measurements of the SDSS DR12 spectra provided by the Portsmouth Group[8] catalog. We classify the sources as quiescent if the S/N of any of the SDSS H$_\alpha$, H$_\beta$, [N II]λ6584, or [O III]λ5007 emission lines used in the BPT is $<$3 (e.g., Secrest & Satyapal 2020). If S/N $\geqslant$ 3, the sources are classified as either star-forming, AGNs, or composite following the same classification as for the MaNGA BPT (see Section 2). We find that 12 out of the 33 sources are classified as AGNs according to the SDSS (single-fiber) BPT, in agreement with the MaNGA BPT classification. However, two of these AGNs have a median MaNGA EW(Hα $\sim$ 2.8 Å) and would be missed by the WHAN diagram classification. To ensure we do not exclude any bona fide AGNs we thus relax the EW(Hα) cut to $>$2.8 Å. The remaining 21 sources out of the 33 are classified as either quiescent, star-forming, or composite. Using IFU MaNGA data we are thus able to identify 23 new AGNs in dwarf galaxies whose AGN

[4] http://www.sdss.org/surveys/manga
[5] https://www.sdss.org/dr15/manga/manga-analysis-pipeline/
[6] https://www.sdss.org/dr16/manga/manga-target-selection/nsa/
[7] Low Ionization Emission Line Region (LINER).
[8] https://www.sdss.org/dr12/spectro/galaxy_portsmouth/

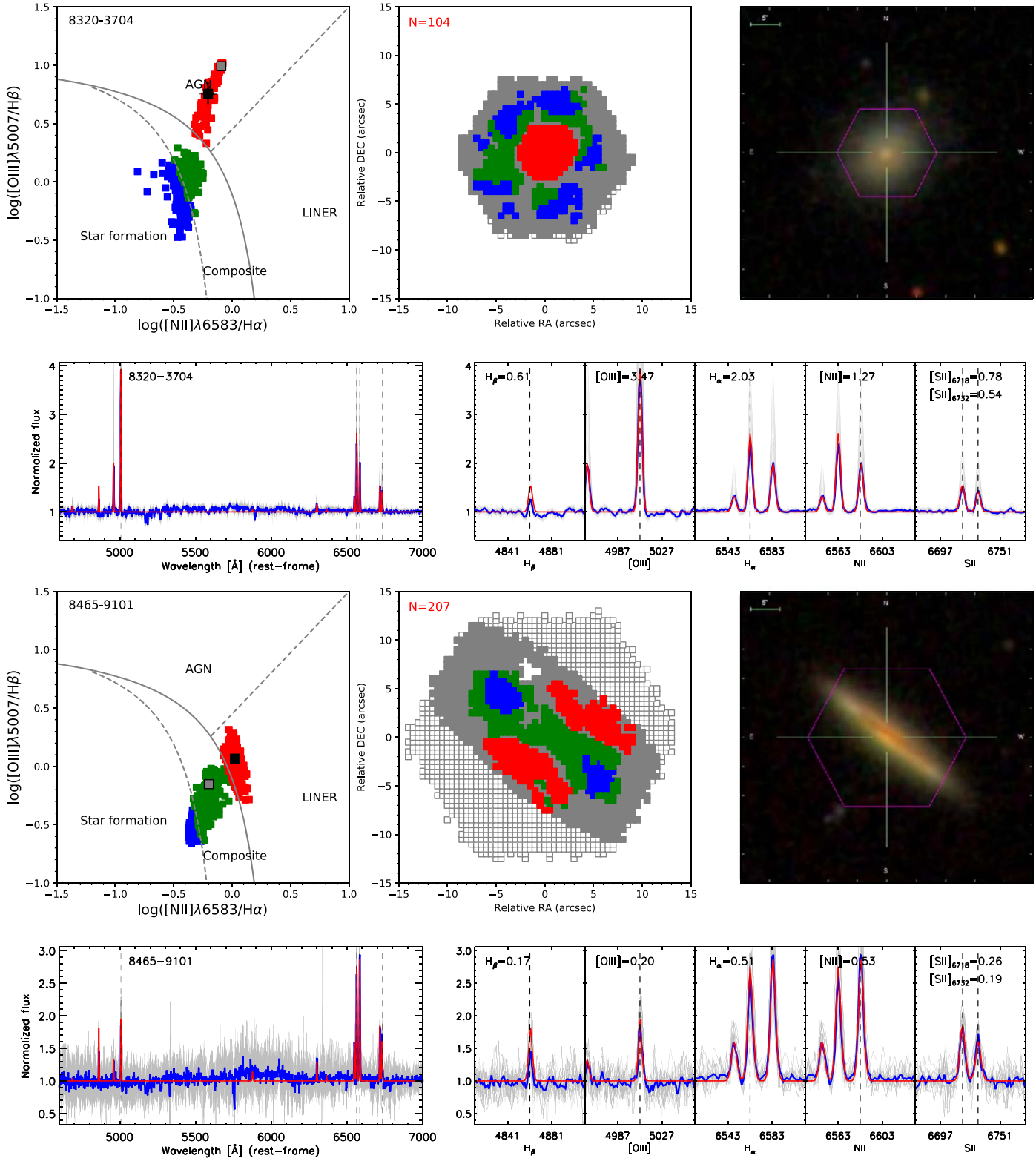

Figure 1. MaNGA analysis for four of the AGN dwarf galaxy candidates. For each source: top left: location of each MaNGA spaxel on the [N II]-BPT used to distinguish between ionization by AGN/LINER (red spaxels), star formation (blue spaxels), or composite (green spaxels). The black square marks the median BPT location of those spaxels classified as AGN/LINER, the gray square the SDSS (single-fiber) BPT location. Top center: spatial distribution of the BPT-classified spaxels (color-coded as in the left panel). Empty squares mark the IFU coverage, gray squares those spaxels with continuum S/N > 1. N shows the number of AGN/LINER spaxels used in the analysis and stacking. Top right: SDSS composite image. The pink hexagon shows the IFU coverage. Bottom left: stacked spectrum (in blue) of all the galaxy spaxels (in gray) which fall in the AGN/LINER region of the BPT diagram. The emission line component is shown in red; bottom right: zoom-in of the stack in the region of the emission lines used in the BPT. The median emission line flux of the AGN/LINER spaxels is shown in units of 10^{-17} erg s^{-1} cm^{-2}.
(The complete figure set (35 images) is available.)

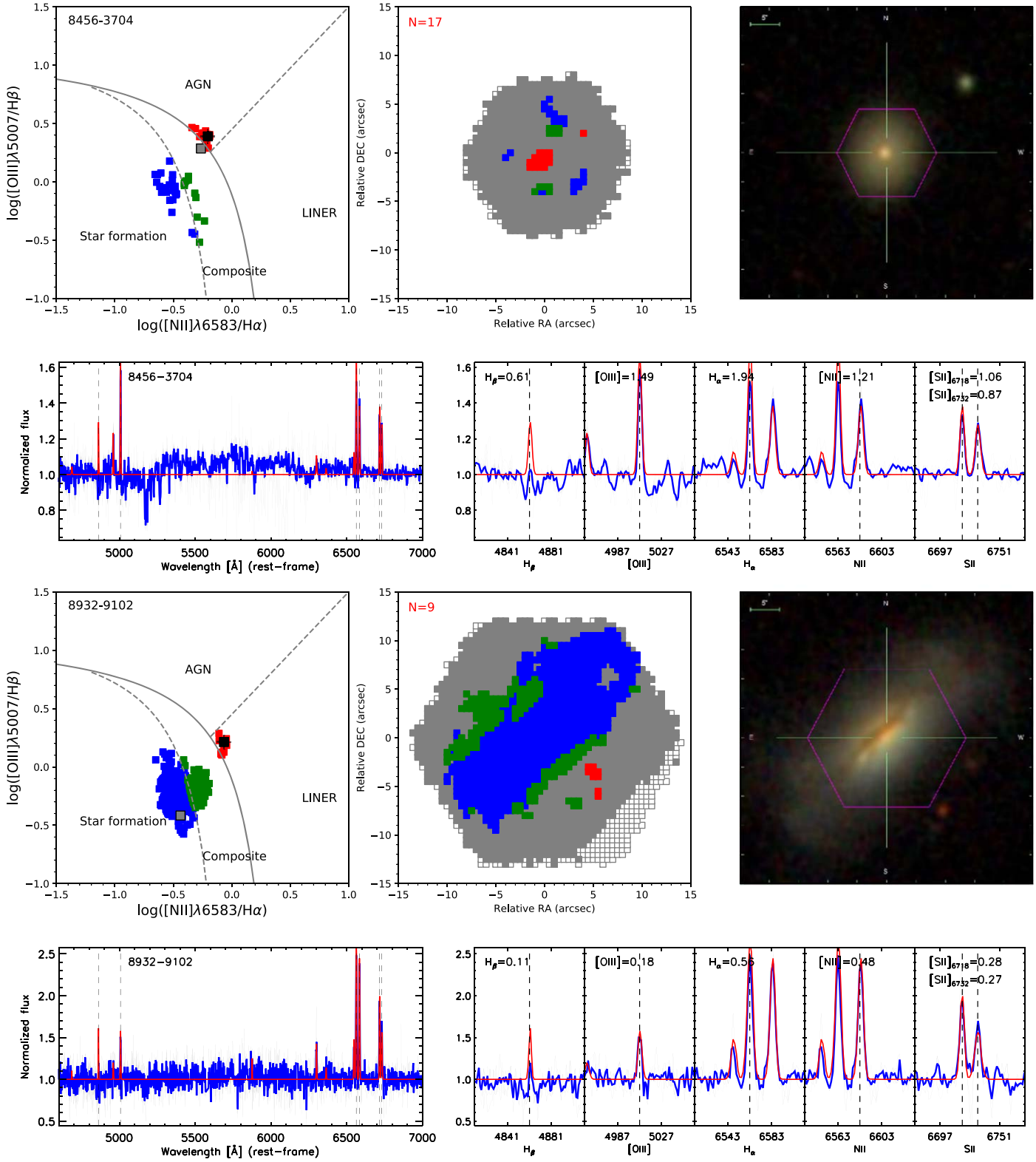

Figure 1. (Continued.)

signatures are hidden (or partly hidden in the case of composite objects) or not available in the BPT of single-fiber SDSS spectra. The use of integrated spectra to search for AGNs can therefore fail in low-mass galaxies, biasing the demographics of dwarf galaxies hosting an AGN (see Section 3.6; e.g., Reines et al. 2013; Cann et al. 2019; Birchall et al. 2020).

3.1. Host Galaxy Properties

The photometric properties of the dwarf galaxies are drawn from the MaNGA PyMorph photometric value -added catalog (MPP-VAC; Fischer et al. 2019), who performed Sérsic and Sérsic+Exponential fits to the 2D surface brightness profiles of

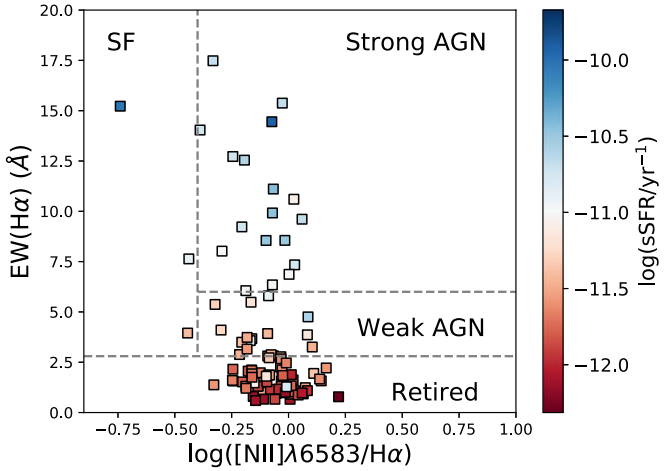

Figure 2. WHAN diagram for the initial 102 dwarf galaxies classified as AGN/LINER according to the [N II]-BPT and [S II]-BPT diagrams. The final sample of AGN dwarf galaxy candidates is formed by the 37 sources classified as strong or weak AGNs in the WHAN diagram. The color bar denotes the median specific star formation rate of the AGN/LINER spaxels.

the MaNGA DR15 galaxy sample. The morphological properties are drawn from the companion catalog, the MaNGA deep learning morphological catalog (MDLM-VAC; Fischer et al. 2019), which provides a morphological classification of the same galaxy sample based on the deep-learning algorithm presented in detail in Domínguez Sánchez et al. (2018). The surface brightness profiles are available for the 37 dwarf galaxies with AGN candidates, 29 of which are best fitted with a Sérsic+Exponential profile or with a Sérsic profile with index $\leqslant 2$. This is in agreement with the late-type classification (i.e., TType > 0 in the MDLM-VAC catalog) of 25 of these sources by the deep-learning-based algorithm. The remaining dwarf galaxies are classified as early-type (TType < 0). The $B-V$ colors derived from the surface brightness profiles range from 0.7 to 1.1, with a median value $\langle B-V\rangle = 0.9$. Such colors are redder than those found by single-fiber optical searches of AGNs in dwarf galaxies (e.g., Reines et al. 2013) and also those of X-ray and radio searches (e.g., Mezcua et al. 2018a, 2019), and are in agreement with the finding that only six out of the 37 IFU AGN candidates are classified as star-forming according to the integrated SDSS BPT (see Table 1). A predominance of star formation over AGN ionization in the central regions seems thus not to be the cause of single-fiber optical diagnostics not being able to fully recover AGN emission in 23 of the 37 AGN candidates. Instead, the AGN emission in most of these sources must be either off-nuclear or turned-off.

3.2. Other Wavelengths

To distinguish between star formation dilution of the AGN ionization, turned-off AGNs, and true off-nuclear wanderers we search for AGN signatures in the mid-infrared, radio, and X-rays. The 37 dwarf galaxies have mid-infrared *WISE* counterparts; however, only two of them are classified as an AGN according to the color cuts of Jarrett et al. (2011): 9000-1901 and 8982-3703, already classified as AGNs based on the SDSS spectrum. In the X-ray regime, no Chandra data are available.

In the radio, seven of the 37 dwarf galaxies have a 1.4 GHz counterpart in the FIRST[9] survey (see Table 1). The peak radio emission ranges from $\sim$1.1 to 20.4 mJy beam^{-1} and is in all cases except for one (8442-1901) resolved. We derive the expected thermal and non-thermal contribution from star formation to the detected 1.4 GHz FIRST radio emission using the correlation for dwarf galaxies of Filho et al. (2019; see also Mezcua et al. 2019). We find that the FIRST radio emission is $\geqslant 3\sigma$ larger than that expected from star formation for all the sources. The star formation contribution to the radio emission ranges from 0.2% to 20.8%. At least $\sim$80% of the radio flux is thus expected to come from an AGN. Most of the dwarf galaxies with FIRST radio emission lack AGN/LINER spaxels at the center of the galaxy, which suggests that either the AGN ionization is diluted by star formation in the central region or that the AGN is switched off. The latter can be now strongly disfavored based on the finding of central AGN radio emission. We note that four out of the seven sources with radio emission are classified as LINERs in the spaxel-averaged BPT, which reinforces not having excluded LINERs from the final sample of AGN dwarf galaxy candidates (Section 2). Higher-resolution radio observations are planned for the sources with a FIRST counterpart in order to confirm the presence of an AGN.

3.3. Off-nuclear Wanderers, Hidden, or Switched-off AGNs?

While the AGN/LINER spaxels of the 14 sources classified as AGNs by the SDSS data are centrally located on the IFU center, for the 23 new AGN candidates most of the AGN/LINER spaxels are offset from the optical center. In the cases with clearly off-nuclear AGN-like line ratios, the emission tends to be diffuse, elongated, and often symmetric, consistent with being light echoes of past AGN activity (e.g., 8083-3704, 8442-1901, 8465-9101; see Figure 1). The switched-off AGN scenario is, however, very unlikely for those sources whose FIRST radio emission is consistent with an AGN origin. In these cases the off-nuclear location of the AGN/LINER spaxels can be rather explained by either star formation dilution (e.g., 8255-12704, 8442-1901, 8465-9101, 8932-9102, 8932-9102; see Figure 1), as supported by the star-forming classification of some of these sources, or the AGN being off-nuclear (e.g., 8932-9102; see Figure 1).

For the off-nuclear AGN candidate 8932-9102, the location of the AGN with respect to the optical center can be derived as the median of the distance between each AGN/LINER spaxel and the IFU center. We find an offset of 6.″4, which corresponds to 2.7 kpc. This offset is consistent with those found in radio (Mezcua et al. 2019; Reines et al. 2020) and X-ray searches (e.g., Mezcua et al. 2018a) of AGNs in dwarf galaxies, and with the (low-luminosity) AGN nature of some ultraluminous X-ray sources (e.g., Mezcua et al. 2013a, 2013b, 2015, 2018b; Kim et al. 2017; Barrows et al. 2019). The offset is also in agreement with simulations of seed black hole formation, which predict that a population of wandering black holes should be present in dwarf galaxies if these have undergone interactions and mergers (e.g., Bellovary et al. 2019).

3.4. AGN Luminosity

The bolometric luminosity ($L_{\rm bol}$) of the 37 AGN candidates can be estimated from the [O III] luminosity ($L_{\rm [O\,III]}$). The latter is derived from the median [O III] flux of the AGN/LINER spaxels and converted to $L_{\rm bol}$ assuming a bolometric correction of 1000 (Moran et al. 2014). We find a range of log $L_{\rm bol} = 38.9$–41.4 erg s^{-1}, which is below the typical AGN

[9] Faint Images of the Radio Sky at Twenty Centimeters.

Table 1
Properties of the 37 AGN Candidates in Dwarf Galaxies

MaNGA Plateifu (1)	R.A. (J2000) (2)	Decl. (J2000) (3)	z (4)	log M_* ($M_\odot$) (5)	log SFR ($M_\odot$ yr^{-1}) (6)	TType (7)	$R_{\rm eff}$ (kpc) (8)	log $L_{\rm bol}$ (erg s^{-1}) (9)	MaNGA BPT (10)	SDSS BPT (11)
7958-9101[a]	258.495841	33.607137	0.039	9.36	−1.32	0.9	3.8	40.8	AGN	AGN
7960-3703	259.183520	32.806265	0.041	9.26	−1.33	−1.3	2.5	39.9	AGN	Star-forming
7990-3702	262.100040	57.002099	0.030	9.16	−1.84	1.6	2.6	39.4	LINER	Quiescent
8083-3704	51.284736	−0.544948	0.038	9.29	−2.17	0.4	2.2	40.0	LINER	Composite
8149-1901	120.221693	28.130394	0.017	9.26	−2.01	−2.1	1.3	40.5	AGN	Composite
8255-12704[a]	165.117740	44.260967	0.025	9.46	−1.21	3.9	4.4	39.3	LINER	Star-forming
8311-3701	203.777234	22.661833	0.032	9.48	−1.98	−1.7	1.6	40.2	AGN	AGN
8320-3702	205.289300	23.277928	0.027	9.30	−1.17	3.5	2.1	39.3	LINER	Star-forming
8320-3704	206.612456	22.076742	0.028	9.01	−1.73	1.0	2.6	40.7	AGN	AGN
8442-1901[a]	199.675905	32.918662	0.036	9.17	−1.02	0.3	1.2	40.2	AGN	Composite
8446-1901	205.753337	36.165656	0.024	9.18	−1.40	−2.1	0.9	40.0	LINER	AGN
8448-12704	166.739672	22.835797	0.023	9.32	−1.44	4.6	4.3	39.2	LINER	Composite
8452-1901	155.885556	46.057755	0.026	9.36	−2.07	2.1	2.0	40.5	AGN	AGN
8453-1901	153.365546	47.516236	0.025	9.40	−1.50	1.0	1.7	39.6	AGN	Composite
8456-12705	151.284662	44.514047	0.026	9.42	−1.06	5.5	7.1	39.3	LINER	Star-forming
8456-3704	150.228406	44.764793	0.028	9.25	−2.11	0.4	2.1	40.4	AGN	Composite
8465-9101[a]	197.580687	47.124056	0.024	9.46	−1.61	3.8	3.7	39.4	LINER	Composite
8466-1901	168.480327	45.488367	0.029	9.38	−2.14	1.3	1.5	40.0	LINER	AGN
8547-6104	219.546188	53.462575	0.038	9.22	−1.75	0.7	2.7	39.9	AGN	Composite
8549-12704	242.978645	46.127727	0.020	9.20	−1.47	3.4	3.4	38.9	LINER	⋯
8588-1901	249.717086	40.199348	0.036	9.18	−1.32	−0.8	1.3	39.6	LINER	Star-forming
8600-6102	244.658478	41.136756	0.038	9.44	−1.70	3.0	3.4	39.6	LINER	Quiescent
8655-6103	355.825111	0.442475	0.037	9.28	−2.28	1.7	2.6	40.5	AGN	AGN
8715-6103	118.872451	52.010499	0.022	9.42	−2.07	3.8	2.9	39.8	AGN	Composite
8720-1901	121.147928	50.708556	0.023	9.39	−1.90	−2.0	1.7	40.6	AGN	AGN
8932-9102[a]	196.651709	27.872946	0.021	9.44	−0.99	4.1	3.5	39.2	LINER	Star-forming
8937-1901	116.997855	29.190689	0.027	8.96	−2.03	1.0	1.6	40.2	AGN	Composite
8982-3703[a]	203.190094	26.580376	0.047	8.88	−0.79	1.1	1.2	41.4	AGN	AGN
8990-12705	173.537567	49.254562	0.037	9.46	−1.28	2.4	2.3	41.0	AGN	AGN
8992-3702	171.657262	51.573041	0.026	9.47	−1.49	1.2	2.4	40.2	AGN	AGN
9000-1901[a]	171.400654	54.382574	0.021	9.27	−0.65	−2.5	1.0	40.2	LINER	AGN
9031-1902	241.029075	44.549765	0.043	9.45	−1.27	−2.0	1.6	40.9	AGN	AGN
9033-3702	222.337719	47.417495	0.026	9.37	−1.54	−0.7	2.2	39.5	LINER	Composite
9035-1901	235.405343	44.272184	0.037	9.14	−2.32	−1.5	1.4	39.7	LINER	Quiescent
9488-1901	126.409848	21.142559	0.023	9.26	−2.19	−2.0	1.2	40.1	LINER	AGN
9865-1902	223.866232	51.047738	0.030	9.13	−2.50	−0.6	1.8	40.1	AGN	Quiescent
9881-1901	204.806913	24.893076	0.028	9.29	−1.88	0.4	1.6	40.4	AGN	⋯

Notes. Column designation: (1) MaNGA plateifu; (2), (3) R.A., decl. coordinates of the optical center of the galaxy or IFU center; (4) galaxy redshift; (5) galaxy stellar mass; (6) galaxy SFR within the IFU field-of-view based on the Hα flux; (7) galaxy TType (>0 for late-type, <0 for early-type); galaxy effective radius; (8) bolometric luminosity of the AGN/LINER spaxels (derived from their median [O III] luminosity); (9) MaNGA (IFU) median BPT classification (derived from the median fluxes of the AGN/LINER spaxels); (9) SDSS (single-fiber) BPT classification.
[a] Galaxy with a FIRST radio counterpart.

bolometric luminosity threshold of $\sim 10^{42}$ erg s^{-1} and indicates that these are low-luminosity AGNs (e.g., Mezcua & Prieto 2014). We note that excluding those sources classified as AGNs by the SDSS BPT, the median bolometric luminosity would be log $L_{\rm bol} = 39.6$ erg s^{-1} (see Figure 3), which is nearly one order of magnitude lower than the median log $L_{\rm bol} = 40.5$ erg s^{-1} of the 14 SDSS AGNs. The $L_{\rm bol}$ is also more than two orders of magnitude lower than those of X-ray- and radio-selected AGNs (Figure 3; e.g., Mezcua et al. 2018a, 2019), which highlights the power of IFU spectroscopy in revealing very faint AGNs in dwarf galaxies.

3.5. Black Hole Mass: Revealing a Hidden Type 1 Low-mass AGN

For three of the SDSS AGNs a black hole mass measurement is reported in the literature (e.g., Reines & Volonteri 2015) based on the width of broad Hα and Hβ emission lines using standard virial techniques: 8446-1901 (log $M_{\rm BH} = 6.52\ M_\odot$), 8992-3702 (log $M_{\rm BH} = 5.99\ M_\odot$), and 9000-1901 (log $M_{\rm BH} = 7.27\ M_\odot$).

The dwarf galaxy 8442-1901 also presents broad Hα emission in the stacked AGN MaNGA spectrum (see Figure B1); however, such a broad component has not been accounted for in the literature (most likely because of its star-forming/composite BPT classification based on the single-fiber SDSS spectrum) nor is it recovered by the MaNGA data-analysis pipeline (see Appendix B). To confirm the AGN BPT classification of 8442-1901 by the MaNGA data we thus perform our own emission line fitting of the Hα + [N II] complex (see the description in Appendix B). As a result we find a broad Hα emission line component of FWHM = 1131 ± 378 km s^{-1}, from which we derive a black hole mass

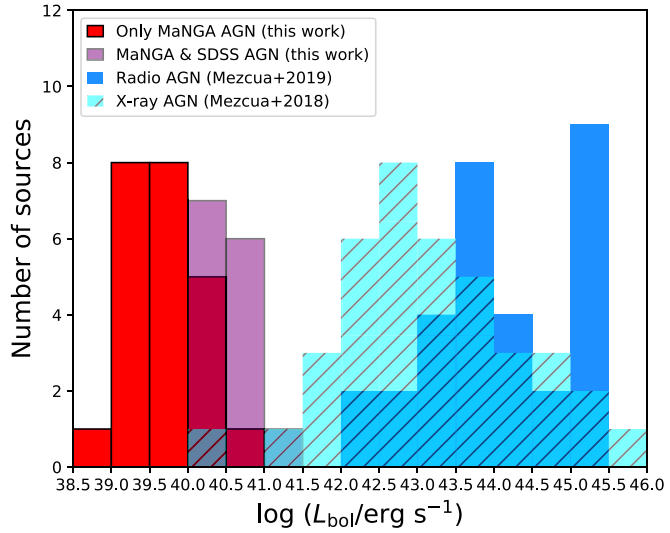

Figure 3. Distribution of bolometric luminosity for the 23 new MaNGA AGN candidates (red bars), the 14 SDSS AGNs (purple bars), the sample of radio AGN dwarf galaxies from Mezcua et al. (2019; blue solid bars), and the X-ray sample of AGN dwarf galaxies from Mezcua et al. (2018b; cyan hashed bars).

log $M_{\rm BH} = 5.07\ M_{\odot}$ (with a typical uncertainty of 0.5 dex) in the IMBH regime. The AGN nature of 8442-1901 is further reinforced by the finding that only 0.9% of its compact FIRST radio emission originates from star formation (see Section 3.2). This indicates that the symmetric, elongated off-nuclear morphology of the AGN spaxels are not light echoes from a switched-off AGN. Instead, the MaNGA data reveal a hidden type 1 AGN in a dwarf galaxy whose central AGN emission is outshone by star formation in the single-fiber (SDSS) BPT diagnostic diagram.

For the remaining 33 AGN dwarf galaxy candidates with no broad Hα or Hβ emission lines we estimate the black hole mass from the stellar velocity dispersion (σ) within 1 $R_{\rm eff}$ applying the $M_{\rm BH}$–σ correlation (e.g., Martín-Navarro & Mezcua 2018; Greene et al. 2019), which should be less biased than the $M_{\rm BH}$–M_{*} correlation (e.g., Shankar et al. 2019; Martín-Navarro et al. 2020). The low-mass end of the $M_{\rm BH}$–σ correlation is found to flatten in some studies (Greene & Ho 2006; Mezcua 2017; Martín-Navarro & Mezcua 2018) but to remain unchanged in others (e.g., Greene et al. 2019), which can be explained by a possible bias toward massive black holes when using only detections (i.e., excluding upper limits) on black hole mass measurements (Greene et al. 2019). We thus estimate the black hole mass using both possibilities: using the correlation from Martín-Navarro & Mezcua (2018) we find a range log $M_{\rm BH} = 5.6$–$6.6\ M_{\odot}$, with 14 sources qualifying as IMBHs (log $M_{\rm BH} < 6\ M_{\odot}$), while using Greene et al. (2019) we find log $M_{\rm BH} = 5.8$–$7.9\ M_{\odot}$ with three sources qualifying as IMBHs. In both cases the Eddington ratios derived as $\lambda_{\rm Edd} = L_{\rm bol}/(M_{\rm BH} \times 1.3 \times 10^{38})$ are $\lambda_{\rm Edd} \leqslant 1\%$, indicating that all the sources are accreting at sub-Eddington rates.

3.6. Demographics

Using MaNGA IFU we find 37 AGN candidates among a sample of 1609 dwarf galaxies with $M_{*} < 3 \times 10^{9}\ M_{\odot}$, which translates into an AGN fraction of 2.3%. This fraction is smaller than the 5.1% of Wylezalek et al. (2018), who investigated 2727 galaxies observed by MaNGA (half of our initial 4718 sources) and found 48 AGNs in dwarf galaxies with $M_{*} < 3 \times 10^{9}\ M_{\odot}$ (Petrosian NSA masses using $h = 0.73$). Although Wylezalek et al. (2018) perform a stringent AGN identification based also on the [N II]-BPT, [S II]-BPT, and WHAN diagrams, many of their AGN candidates are not included in our sample due to their low number of AGN/LINER spaxels. Rembold et al. (2017) and Sánchez et al. (2018) also searched for AGNs using MaNGA, but both works focus on the central region of galaxies and thus do not include most of the light-echoes and off-nuclear AGN dwarf galaxy candidates found here. Penny et al. (2018) used the MaNGA survey to investigate AGNs in dwarf galaxies, but they performed a different procedure to ours, applying first the WHAN diagram to the whole integrated spectrum covered by MaNGA (and not only to the AGN/LINER spaxels) in order to identify quenched galaxies and plotting later the BPT diagram to find AGNs in these sources. As a result, only one (8982-3703) of their six AGN dwarf galaxies is included in our final sample of AGN candidates.

Among single-fiber spectroscopic studies, one of the largest searches for AGNs in dwarf galaxies is that of Reines et al. (2013), who identified 136 AGN/composite objects in the [N II]-BPT and [S II]-BPT diagrams among a sample of 25974 SDSS dwarf galaxies with $M_{*} < 3 \times 10^{9}\ M_{\odot}$. Excluding composite objects, only 17 of their AGNs qualify as such by the WHAN diagram, which translates into an AGN fraction of ∼0.1%. This is significantly smaller than our AGN fraction, which we attribute to the bias of single-fiber spectroscopy toward central AGNs. Indeed, considering only the 14 SDSS AGNs, we would have an AGN fraction of ∼0.9%, closer to that of the single-fiber SDSS studies but lower than that of the whole MaNGA AGN dwarf galaxy sample, which emphasizes the power of IFU in demographic studies of AGNs in dwarf galaxies.

4. Conclusions

Using MaNGA IFU data we have identified a sample of 37 AGN candidates in dwarf galaxies. In 23 of them the AGN ionization signatures are largely missed by single-fiber (SDSS) spectroscopy, which classifies them as either quiescent, star-forming, or composite. While this suggests that star formation is the dominant source of ionization in the central region, most of the galaxies are not star-forming. The AGNs could thus be either switched off or wandering in the host dwarf galaxy, as predicted by models of seed black hole formation. A black hole mass $\sim 10^{5}\ M_{\odot}$ is derived for one of the 23 new AGN candidates based on the detection a broad Hα emission line component, which constitutes the first hidden type 1 low-mass AGN to be revealed by IFU data. The AGN bolometric luminosity of the 23 new AGN candidates is $\lesssim 10^{40}$ erg s^{-1}, nearly one order of magnitude fainter than that of the dwarf galaxies with single-fiber AGN emission and several orders of magnitude lower than that of X-ray and radio AGN dwarf galaxies. IFU surveys offer thus a potential tool for identifying hidden and faint AGNs, which is crucial for population studies of AGNs in dwarf galaxies and for understanding whether these host the seed black holes of the early universe. The detailed kinematic an stellar population properties of the sample will be presented in a forthcoming paper, while radio and X-ray observations are planned to confirm the AGN nature.

The authors would like to thank they anonymous referee for his/her helpful comments. M.M. would like to thank

A. Olmo-García for sharing her emission line fitting code, S. Sánchez for helpful discussions, and D. Wylezalek for sharing the stellar masses of her AGN sample. H.D.S. thanks M. Bernardi for her help with the stacking spectra procedure. M.M. acknowledges support from the Beatriu de Pinos fellowship (2017-BP-00114). H.D.S. acknowledges support from the Centro Superior de Investigaciones Científicas PIE2018-50E099.

Appendix A
Stacking

For each individual galaxy, the spectra of all the spaxels that fall in the AGN/LINER region are stacked together. We use the HYB10-GAU-MILESHC maps from the MaNGA DR15, which provide the observed flux, the emission line component, the stellar continuum, and the best-fitting model. We stack both the observed flux (in blue in Figures 1, B1 and B2) and the emission line components (shown in red) to better visualize the emission line fluxes. The stacking procedure is performed as follows: the spectra are first rest-frame corrected (including the redshift and the correction due to the rotational velocity) and then the wavelengths are converted to air units following the standard convention. The flux is normalized in two regions free of emission lines in the blue and red part of the spectrum (4600–4700; 6780–6867 Å) to remove the intrinsic slope of the spectra. The stacked spectrum is computed as the median value of the 3σ clipped flux at each wavelength. The emission line component is shifted by 1 to match the observed flux. Skylines or masked wavelength regions are not used in the stacking (see Domínguez Sánchez et al. 2019 for additional details).

Appendix B
Broad Emission Line Measurements

We perform a visual inspection of all the AGN/LINER candidates in order to check the consistency of the emission line measurements provided by the MaNGA data-analysis pipeline. The visual inspection of the stacked spectrum of 8442-1901 shows that the MaNGA emission line model seems not to correctly fit the emission lines used in the BPT diagnostic diagram, which could be biasing its BPT classification as an AGN (see Figure B1). This is likely due to the possible presence of a broad Hα emission line component in the stacked AGN spectrum of 8442-1901. To probe this, we perform a multi-Gaussian fit to the Hα+[N II] complex (and also of the Hβ and [O III] emission lines used in the BPT diagram) using the Python package LMFIT as in Olmo-García et al. (2017). We follow the common procedure (e.g., Reines et al. 2013) of assuming the same width for the [N II]λ6583, [N II]λ6548, [O III]λ5007, [O III]λ4958, narrow Hα, and narrow Hβ emission line Gaussian components and allowing for a secondary broad Hα and Hβ component. The relative separations between the centers of the narrow components are fixed using their theoretical wavelengths and the flux ratios of the [N II] and [O III] doublets are set to the theoretical values of 3.06 and 2.99, respectively. The best model (that with the lowest χ^2) is obtained when including a broad Hα component but no Hβ broad component (see Figure B1, bottom). The resulting FWHM is corrected for instrumental resolution, thermal and natural broadening, which yields a FWHM (broad Hα) $= 1131 \pm 378$ km s^{-1}. This, together with the luminosity (log L(Hα) $= 38.6$ erg s^{-1}) derived from the flux of the broad Hα component, allows us to derive a black hole mass under the assumption that the broad-line region from which the broad Hα originates is virialized. Using a geometrical factor $\epsilon = 1$ (Equation (5) in Reines et al. 2013), we find log $M_{\rm BH} = 5.07$ $M_{\odot}$ (with a typical uncertainty of 0.5 dex). The resulting BPT classification, based on the derived narrow emission lines fluxes of the Hα, Hβ, [N II]λ6583, and [O III]λ5007, is shown as a yellow star in Figure B1 (top left panel) and confirms the AGN classification of 8442-1901.

For 8446-1901 the MaNGA emission line model seems, as for 8442-1901, not to correctly fit the Hα+[N II] emission line complex due to the presence of a broad Hα emission line component already present in the SDSS spectrum (see Figure B2). To confirm the AGN BPT classification of MaNGA we thus also perform a multi-Gaussian fit of the Hα +[N II] complex that includes a broad Hα component (Figure B2, bottom). We find FWHM (broad Hα) $= 3116 \pm 205$ km s^{-1} and log $M_{\rm BH} = 5.73$ $M_{\odot}$. Using the narrow emission line fluxes of Hα and [N II]λ6583, 8442-1901 is classified as an AGN/LINER in the BPT diagram (yellow star in the top left panel of Figure B2).

The BPT diagram and stacked spectrum of the 35 AGN dwarf galaxy candidates not shown here in the appendix are available in the figure set of Figure 1.

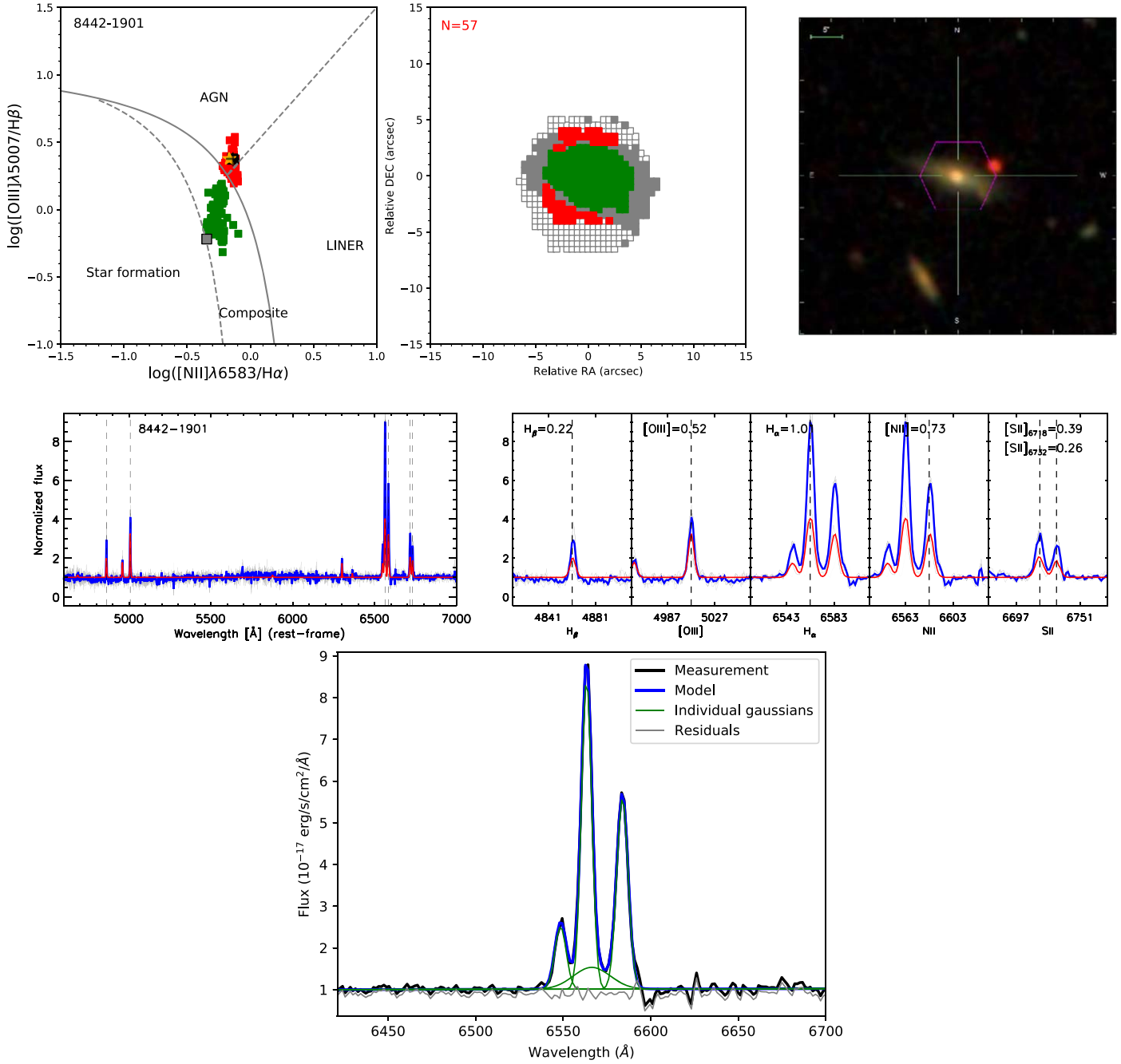

Figure B1. Same caption as in Figure 1. The yellow star marks the median BPT location based on the fluxes derived from the multi-Gaussian fitting of the stacked spectrum of the AGN/LINER spaxels. Bottom: multi-Gaussian emission line fitting of the Hα+[N II] complex of the stacked spectrum.

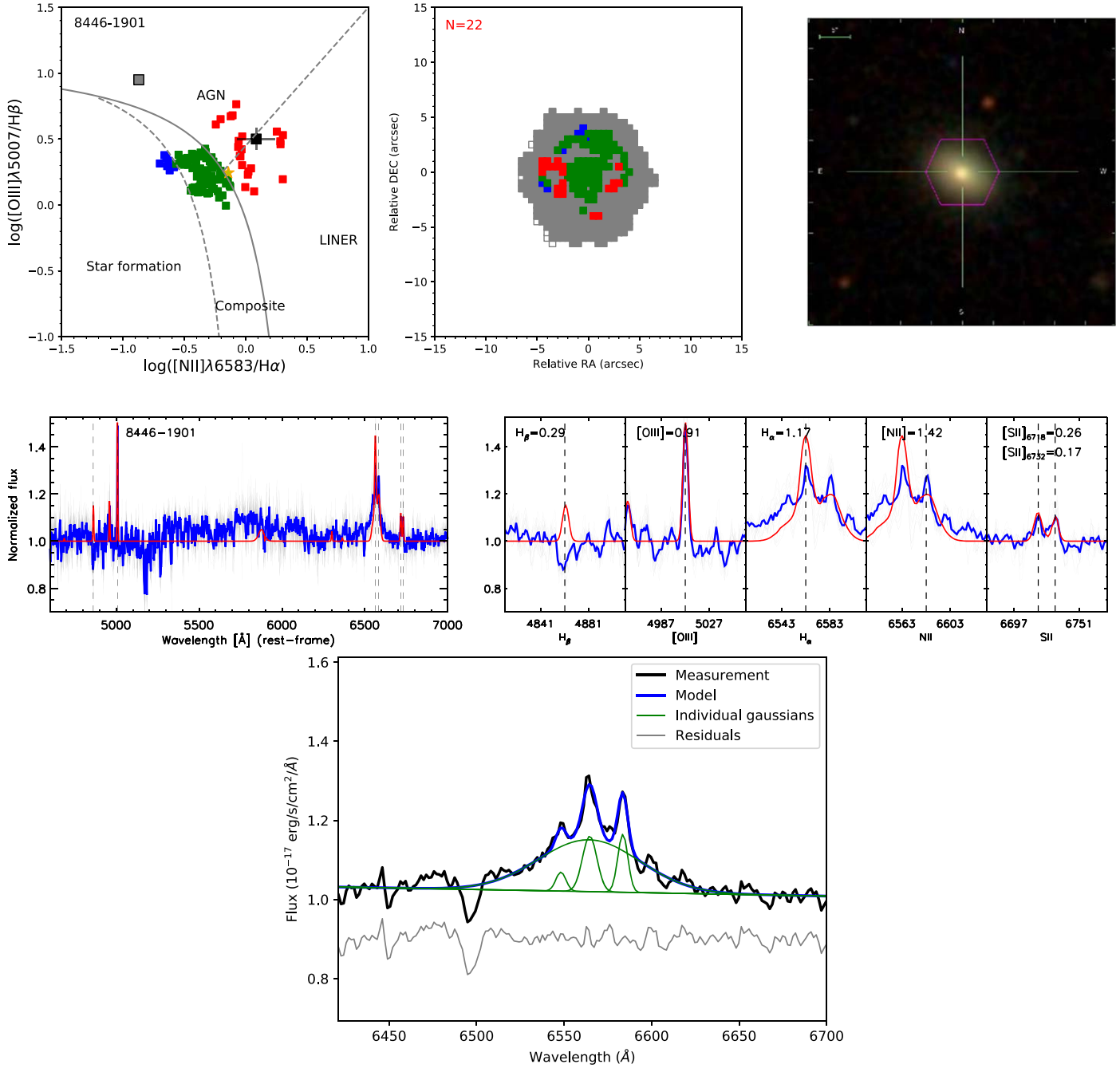

Figure B2. Same caption as for Figure 1. The yellow star marks the median BPT location based on the fluxes derived from the multi-Gaussian fitting of the stacked spectrum of the AGN/LINER spaxels. Bottom: multi-Gaussian emission line fitting of the Hα+[N II] complex of the stacked spectrum.

ORCID iDs

Mar Mezcua https://orcid.org/0000-0003-4440-259X

References

Baldassare, V. F., Geha, M., & Greene, J. 2018, ApJ, 868, 152
Baldassare, V. F., Geha, M., & Greene, J. 2020, ApJ, 896, 10
Baldwin, J. A., Phillips, M. M., & Terlevich, R. 1981, PASP, 93, 5
Barrows, R. S., Comerford, J. M., & Greene, J. E. 2018, ApJ, 869, 154
Barrows, R. S., Mezcua, M., & Comerford, J. M. 2019, ApJ, 882, 181
Bellovary, J. M., Cleary, C. E., Munshi, F., et al. 2019, MNRAS, 482, 2913
Birchall, K. L., Watson, M. G., & Aird, J. 2020, MNRAS, 492, 2268
Bundy, K., Bershady, M. A., Law, D. R., et al. 2015, ApJ, 798, 7
Cann, J. M., Satyapal, S., Abel, N. P., et al. 2019, ApJL, 870, L2
Cid Fernandes, R., Stasińska, G., Schlickmann, M. S., et al. 2010, MNRAS, 403, 1036
Comerford, J. M., & Greene, J. E. 2014, ApJ, 789, 112
Dickey, C. M., Geha, M., Wetzel, A., & El-Badry, K. 2019, ApJ, 884, 180
Domínguez Sánchez, H., Bernardi, M., Brownstein, J. R., Drory, N., & Sheth, R. K. 2019, MNRAS, 489, 5612
Domínguez Sánchez, H., Huertas-Company, M., Bernardi, M., Tuccillo, D., & Fischer, J. L. 2018, MNRAS, 476, 3661
Filho, M. E., Tabatabaei, F. S., Sánchez Almeida, J., Muñoz-Tuñón, C., & Elmegreen, B. G. 2019, MNRAS, 484, 543
Fischer, J. L., Domínguez Sánchez, H., & Bernardi, M. 2019, MNRAS, 483, 2057
Greene, J. E., & Ho, L. C. 2006, ApJL, 641, L21
Greene, J. E., Strader, J., & Ho, L. C. 2019, arXiv:1911.09678

Jarrett, T. H., Cohen, M., Masci, F., et al. 2011, ApJ, 735, 112
Kauffmann, G., Heckman, T. M., Tremonti, C., et al. 2003, MNRAS, 346, 1055
Keel, W. C., Maksym, W. P., Bennert, V. N., et al. 2015, AJ, 149, 155
Kewley, L. J., Dopita, M. A., Sutherland, R. S., Heisler, C. A., & Trevena, J. 2001, ApJ, 556, 121
Kewley, L. J., Groves, B., Kauffmann, G., & Heckman, T. 2006, MNRAS, 372, 961
Kim, M., Ho, L. C., & Im, M. 2017, ApJL, 844, L21
Martín-Navarro, I., Burchett, J. N., & Mezcua, M. 2020, MNRAS, 491, 1311
Martín-Navarro, I., & Mezcua, M. 2018, ApJL, 855, L20
Mezcua, M. 2017, IJMPD, 26, 1730021
Mezcua, M. 2019, NatAs, 3, 6
Mezcua, M. 2020, arXiv:2004.11911
Mezcua, M., Civano, F., Fabbiano, G., Miyaji, T., & Marchesi, S. 2016, ApJ, 817, 20
Mezcua, M., Civano, F., Marchesi, S., et al. 2018a, MNRAS, 478, 2576
Mezcua, M., Farrell, S. A., Gladstone, J. C., & Lobanov, A. P. 2013a, MNRAS, 436, 1546
Mezcua, M., Kim, M., Ho, L. C., & Lonsdale, C. J. 2018b, MNRAS, 480, L74
Mezcua, M., & Prieto, M. A. 2014, ApJ, 787, 62
Mezcua, M., Roberts, T. P., Lobanov, A. P., & Sutton, A. D. 2015, MNRAS, 448, 1893
Mezcua, M., Roberts, T. P., Sutton, A. D., & Lobanov, A. P. 2013b, MNRAS, 436, 3128
Mezcua, M., Suh, H., & Civano, F. 2019, MNRAS, 488, 685
Moran, E. C., Filippenko, A. V., & Chornock, R. 2002, ApJL, 579, L71
Moran, E. C., Shahinyan, K., Sugarman, H. R., Vélez, D. O., & Eracleous, M. 2014, AJ, 148, 136
Olmo-García, A., Sánchez Almeida, J., Muñoz-Tuñón, C., et al. 2017, ApJ, 834, 181
Penny, S. J., Masters, K. L., Smethurst, R., et al. 2018, MNRAS, 476, 979
Reines, A. E., Condon, J. J., Darling, J., & Greene, J. E. 2020, ApJ, 888, 36
Reines, A. E., Greene, J. E., & Geha, M. 2013, ApJ, 775, 116
Reines, A. E., & Volonteri, M. 2015, ApJ, 813, 82
Rembold, S. B., Shimoia, J. S., Storchi-Bergmann, T., et al. 2017, MNRAS, 472, 4382
Ricarte, A., & Natarajan, P. 2018, MNRAS, 481, 3278
Sánchez, S. F., Avila-Reese, V., Hernandez-Toledo, H., et al. 2018, RMxAA, 54, 217
Schawinski, K., Thomas, D., Sarzi, M., et al. 2007, MNRAS, 382, 1415
Secrest, N., & Satyapal, S. 2020, arXiv:2005.06452
Shankar, F., Bernardi, M., Richardson, K., et al. 2019, MNRAS, 485, 1278
van Wassenhove, S., Volonteri, M., Walker, M. G., & Gair, J. R. 2010, MNRAS, 408, 1139
Wylezalek, D., Zakamska, N. L., Greene, J. E., et al. 2018, MNRAS, 474, 1499